

# Predicting Terrain Traversability from Thermal Diffusivity

Chris Cunningham, Uland Wong, Kevin M. Peterson, William L. “Red” Whittaker

**Abstract** This paper presents a method to predict soil trafficability by estimating the thermal diffusivity of terrain using a moving, continuous-wave laser. This method enables differentiation between different densities on the same material, which vision-based methods alone cannot achieve. The bulk density of a granular material has a significant effect on its strength. This approach fits the thermal response as effected by a laser to an analytical model that is dependent on thermal diffusivity. Experimental soil strength measurements validate that thermal diffusivity is a predictor of trafficability for a given material.

## 1 Introduction

This paper presents a technique for determining terrain traversability from measurements of thermal diffusivity. Classical perception approaches detect material shape and appearance, but cannot measure the underlying properties that determine trafficability. The inability to characterize these non-geometric properties are a primary cause of robotic failure on Mars, the Moon, and Earth. Spirit ended its mission mired in soft soil; Lunokhod was entrapped by loose soil while entering a crater [1]. Means to predict these conditions would transform how planetary rovers operate, increasing both safety and efficiency.

This research seeks to predict the mechanical behavior of granular soils by sensing their thermal properties. The mechanical behavior and trafficability of granular soils is primarily governed by particle size distribution, particle shape, bulk density,

---

Chris Cunningham, Uland Wong, Kevin M. Peterson, and William L. “Red” Whittaker  
Robotics Institute, Carnegie Mellon University, 5000 Forbes Ave, Pittsburgh, PA 15213, e-mail: ccunningham@cmu.edu, uyw@andrew.cmu.edu, kp@cs.cmu.edu, red@cmu.edu

Kevin M. Peterson  
Astrobotic Technology Inc., 2515 Liberty Ave., Pittsburgh, PA 15222, e-mail: kevin.peterson@astrobotic.com

and relative density [2]. Shape and density distribution are principle parameters determining the range of soil strength while bulk and relative density modulate the strength [3] [4]. Compact materials with higher bulk density are much stronger than loose materials with low bulk density.

Bulk density and porosity of a soil also have a strong influence on the specific heat, volumetric heat capacity, and thermal diffusivity of granular media [5]. Compact soils with higher bulk density and lower void ratio conduct heat more easily between particles. Likewise, loose soils with lower bulk density and higher void ratio have lower thermal conductivity and diffusivity [6] [7]. Therefore, because material density influences both the mechanical and thermal properties of granular materials, thermal diffusivity is correlated with the mechanical behavior of a soil.

This paper presents a method for detecting the difference between traversable, compact soil and loose, hazardous soil by remotely estimating thermal diffusivity of terrain. A continuous-wave laser and a thermal camera are co-located, pointed at a granular material, and translated with respect to that material. The laser introduces a thermal transient as it moves across the terrain. The thermal camera observes the resulting temperatures.

Section 2 discusses related work in non-geometric hazard detection and thermal diffusivity estimation. Section 3 presents an analytical model to estimate thermal diffusivity based on the transient temperature response of a granular material to heat flux from a moving laser. Specifics of the experiments conducted and results are presented in Section 4 and analyzed in Section 5. In Section 6, theoretical correlations of diffusivity to bulk density and traversability are validated using soil strength measurements. Section 7 discusses conclusions and directions for future research.

## 2 Related Work

Prior work on non-contact identification of non-geometric terrain hazards has primarily focused on vision-based methods. These methods have shown promise but are limited to sensing surface appearance, which is not necessarily correlated with the bulk characteristics of a material. This research enables differentiation between different preparations of the same soil, which can have very different interactions with wheels though they may appear identical on the surface. It builds upon prior research in photothermal radiometry to develop a method for diffusivity estimation that is viable for integration into an autonomous vehicle.

Helimick, Angelova, and Matthies use visual texture and depth from stereo imagery to classify terrain. Data from multiple sensors are combined to make the classification, but the classes are determined by an encoding of domain knowledge [8]. These approaches have been extended using computer vision to predict correlated terrain properties. These vision techniques operate on the principle that terrain with similar appearance has a similar response. Terrain response (either by driving or soil testing) is measured and visual appearance in the area of those measurements

is recorded. Based on this information, self-supervised learning is used to map upcoming appearance to likely terrain types. These terrain types are characterized by typical response.

Although vision-based predictive models progress towards alerting robotic systems to variation in terrain, they are fundamentally limited. The surface appearance of a patch of terrain is not necessarily directly correlated with its bulk physical characteristics. While appearance can be used to associate similar terrain, it cannot measure important characteristics such as compaction, which is a critical factor in determining shear strength. As a result, terrain patches with similar appearance, but dissimilar compositions, and therefore trafficability, have an ambiguous classification when based on visual data alone.

In the applied physics community, the problem of estimating the thermal diffusivity of a material is well researched. Photothermal radiometry is a widely used technique for non-contact estimation of the thermal properties of thin films using an infrared detector and a single laser flash [9] [10]. This method is most effective with a thin film but has been applied to layered materials as well as powders where it can detect a difference between loose and consolidated powders [11]. Though these methods are effective in a laboratory environment, they require precisely-calibrated, sensitive instruments that are not feasible to implement on mobile robots.

Multi-spectral imaging in visible and IR wavelengths has been used for terrain classification with demonstrated success in identification of vegetation [12]. In addition, thermal imaging from a Mars orbiter has been used to estimate the thermal inertia and subsequently the density of the soil in order to estimate mechanical properties of soil in potential Mars Exploration Rover landing sites. Unfortunately, the resolution of thermal images from orbiting satellites is too low for reliable application to rover mobility [13].

This research is distinct from the methods above in two important ways. First, this approach probes deeper than vision-based methods alone that are limited to prediction solely from observation of surface appearance. Second, this method for thermal diffusivity measurement is viable for mobile robots. This method does not require the highly calibrated experimental setups used in photothermal radiometry for thin films. In addition, it provides high resolution at the scale of a robot that satellite imagery cannot.

### 3 Thermal Diffusivity Estimation

The approach for measuring thermal diffusivity estimation is macroscopic measurements of the transient temperature response caused by a low-power, continuous-wave, semiconductor laser. The laser is pointed at the soil while a thermal camera measures the temperature response of the terrain to the laser excitation. The camera and the laser are translated linearly, parallel to the ground at a constant velocity. The thermal diffusivity of the soil is estimated by fitting parameters of a known model to the transient thermal response of the material to the laser.

### 3.1 Analytical Model

The mathematical model of the thermal response is derived from the three-dimensional heat diffusion equation, which governs heat flow.

$$\frac{\partial \theta}{\partial t} = k \left( \frac{\partial^2 u}{\partial x^2} + \frac{\partial^2 u}{\partial y^2} + \frac{\partial^2 u}{\partial z^2} \right) \quad (1)$$

$\theta$  is the temperature at a point  $(x, y, z)$  in a Cartesian coordinate system, and  $k$  is the thermal diffusivity of the material. The material under test is modeled as a semi-infinite plane extending from  $z = 0$  in the negative  $z$  direction. The diffusion equation is subject to a Neumann boundary condition at  $z = 0$ .

$$\frac{\partial \theta}{\partial z} = 0, z = 0 \quad (2)$$

This boundary condition makes the assumption that there is no heat lost at the sample surface [10]. The incident heat from the laser is modeled as a Gaussian instead of a uniform distribution, which is more physically accurate and allows for some helpful mathematical simplifications [14].

$$Q(x', y', z', t') = \frac{P}{2\pi r^2} \exp\left(-\frac{(x' - vt')^2 + y'^2}{2r^2}\right) \delta(z') \quad (3)$$

$Q$  represents a Gaussian laser in the plane  $z = 0$  moving along the  $x$ -axis at  $y = 0$ .  $P$  is the total power from the laser absorbed by the material,  $v$  is the velocity of the laser in the  $x$  direction, and  $r$  is the radius of the laser spot. Because this problem is addressed macroscopically and the absorption depth of the laser is very shallow, it is assumed that all of the power from the laser is absorbed at the surface of the material [15]. The Green's function for a point source in three-dimensions subject to the boundary condition given above is used to find the equation for the temperature at a point  $(x, y, z)$ . This Green's function is given by Carslaw and Jaeger [16] and represents the temperature of a point  $(x, y, z, t)$  in response to a unit point source at  $(x', y', z', t')$ .

$$G(x, y, z, t, x', y', z', t') = \frac{1}{4(\pi k(t - t'))^{\frac{3}{2}}} \exp\left(-\frac{(x - x')^2 + (y - y')^2 + (z - z')^2}{4k(t - t')}\right) \quad (4)$$

The equation for the heat flow from the laser is used in conjunction with the Green's function to find the temperature at any  $(x, y, z, t)$  due to the laser excitation. An offset  $\theta_0$  is added to represent the initial temperature before laser excitation.

$$\theta(x, y, z, t) = \int_{-\infty}^t \int_{-\infty}^{\infty} \int_{-\infty}^{\infty} \int_{-\infty}^{\infty} Q(x', y', z', t') G(x, y, z, t, x', y', z', t') dz' dy' dx' dt' + \theta_0 \quad (5)$$

This solution is simplified using the recipricocity and translation properties of Green's functions and the fact that the integrals over  $x'$  and  $y'$  can be simplified to gaussian forms, which result in known solutions. The final result is a formula for the temperature at  $(x, y, z, 0)$  [17].

$$\theta(x, y, z, 0) = P \int_0^\infty \frac{\exp\left(-\frac{(x+vt')^2+y^2}{2r^2+4kt'} - \frac{z^2}{4kt'}\right)}{\sqrt{\pi^3 kt' (2r^2 + 4kt')}} dt' + \theta_0 \quad (6)$$

Thus, the temperature at  $(x, y, z, 0)$  is only a function of a few variables.  $\theta_0$  can be easily measured from a thermal camera before the laser excitation. In this paper,  $v$  is experimentally controlled.  $r$  is estimated by calibrating the laser. The two unknown variables are the thermal diffusivity of the material under test,  $k$ , and the amount of power absorbed by the material,  $P$ , which is a function of both the laser and the material.

### 3.2 Diffusivity Estimation

To estimate the thermal diffusivity constant of a material, data is extracted from a thermal image to directly correspond to  $\theta_x$ , which is the model (6) evaluated at  $y = 0, z = 0$ , and  $t = 0$ .

$$\theta_x(x; x_{off}, P, k) = P \int_0^\infty \frac{\exp\left(-\frac{(x+x_{off}+vt')^2}{2r^2+4kt'}\right)}{\sqrt{\pi^3 kt' (2r^2 + 4kt')}} dt' + \theta_0 \quad (7)$$

An example thermal image is shown in Figure 1. The maximum temperature in the  $y$  direction occurs along the  $x$ -axis at  $y = 0$ , so it is straightforward to extract the maximum temperature in the  $y$  direction for every pixel column. These are  $(x, \theta_x(x))$  data points, where translational alignment of the  $x$  values with the model is still ambiguous. To align the data points with the model, all  $x$  values are translated so that  $x = 0$  corresponds to the maximum  $\theta_x$  value. Pixel distances are scaled to the equivalent linear distance on the material.

Unfortunately, assuming that the maximum occurs at  $x = 0$  is only an approximation. With low velocity, high diffusivity, and a small laser spot radius, the temperature response is nearly symmetric about the  $y$ -axis with a maximum at  $x = 0$ . However, as the quantity  $vr/k$  increases, the response becomes less symmetric, and the maximum of the curve shifts towards more negative values of  $x$ . Thus the maximum value in the  $x$ -direction is not easily predicted as it is dependent on the velocity and radius of the laser as well as the diffusivity of the material under test [18] [14] [19]. For the velocities, diffusivities, and radii considered in this paper, the maximum occurs close enough to make the approximation that it is at  $x = 0$ . In (7),  $x_{off}$  is an offset value used to compensate for errors in  $x$ -alignment. First is the error that occurs through the assumption that the position of the maximum temperature cor-

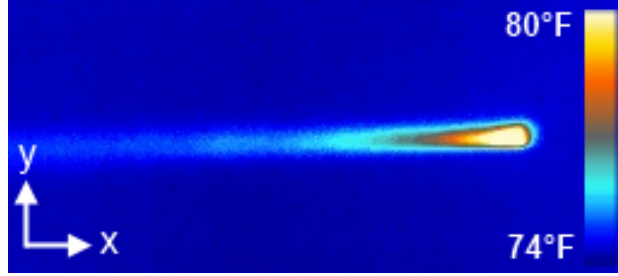


Fig. 1: Thermal transient produced by a 100mW 532nm laser being translated at a constant velocity on a loose preparation of JSC-1A

responds to  $x = 0$ , when in fact it does not. Second is error that arises when the resolution of the camera is not high enough to precisely capture the  $x$  value of the maximum temperature of the thermal response.

The resulting (position, temperature) data points are used to fit (7). The three parameters are  $x_{off}$ ,  $P$ , and  $k$ .  $\theta_0$  is estimated from the mean temperature of the surrounding material.  $r$  is estimated before the experiment through analysis of a laser pulse [20].  $v$  is known as it is controlled by the experimental setup. An optimization algorithm (e.g. Nelder Mead) is used to minimize the root mean square error (RMSE) between the experimental data and (7) evaluated at estimates of  $x_{off}$ ,  $P$ , and  $k$ .

$$(x_{off}, P, k) = \underset{x_{off}, P, k}{\operatorname{argmin}}(RMSE(\theta(x; x_{off}, P, k))) \quad (8)$$

Thermal diffusivity,  $k$ , can then be used to detect when the material type or density of the terrain has changed. For a given material, a lower diffusivity corresponds to a lower bulk density and therefore less traction. Likewise, a higher diffusivity corresponds to a higher bulk density and therefore more traction. Thus, by measuring the thermal response of terrain to a laser excitation, thermal diffusivity can be estimated and used as a predictor of trafficability.

## 4 Experimental Results

In order to test the methodology and observe the phenomena this paper describes, three lunar regolith simulants were used for these experiments, JSC-1A, BP-1, and GRC-1. JSC-1A is the gold standard for lunar regolith simulants and is widely available for research purposes [21]. BP-1 is a lunar regolith simulant that is very similar in its major elements to JSC-1A. However, its minor elemental composition precludes it from closely simulating lunar regolith chemical composition, which has a large impact on thermal properties. It does, however, closely simulate the geotechnical properties including particle size and shape distribution [22]. GRC-1 is a lunar

regolith simulant specifically developed to be an inexpensive simulant of the mobility properties of lunar terrain and does not replicate all of the mechanical properties nor the chemical composition. It does not have a wide range of compaction and has a low thermal diffusivity compared to the other two simulants [23].

All three simulants were used in both loose and compact preparations. Loose preparation consisted of pouring the material into the sample container, hand agitation with a shovel, and gentle leveling to create a flat surface. Compact preparation utilized a hydraulic press on a flat steel plate top until maximum pressure was achieved as shown in Figure 2.

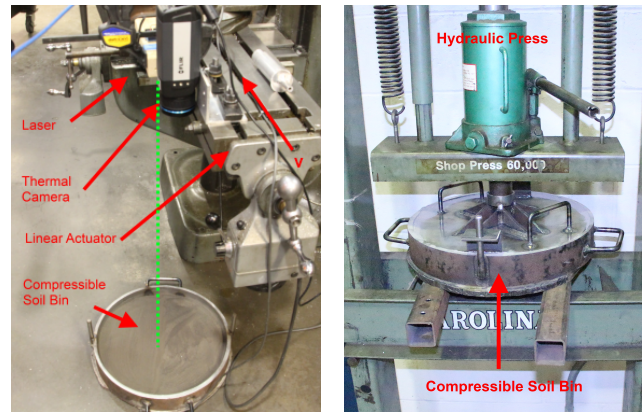


Fig. 2: Experimental setup for thermal diffusivity experiments (left). A 100mW 532nm continuous-wave laser and a thermal camera are mounted to a linear actuator and translated a constant velocity parallel to a soil sample below. A hydraulic press (left) and compressible soil bin with lid are used to repeatedly prepare compressed soil samples.

Data to validate thermal diffusivity estimation was collected using a controlled setup shown in Figure 2. A thermal camera and a continuous-wave 100mW 532nm laser were mounted to a linear mill and pointed down at a soil bin containing either a loose or compact simulant. The thermal camera recorded images at 7hz. The mill was driven at 2.5 mm/s, 3.8 mm/s, 5.1 mm/s, and 6.4 mm/s. The laser point was translated .25 m, from one end of the soil bin to the other.

The experimental data was fit to the model (7) using the parameters  $k$ ,  $P$ , and  $x_{off}$ . Example curves are shown in Figure 3. The blue points are the measured temperatures and the red line is the analytical model.

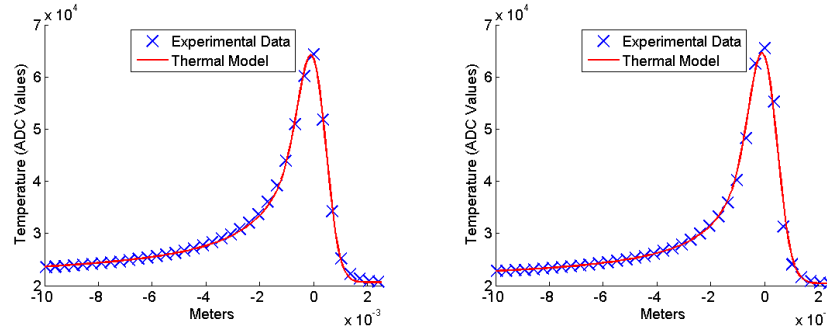


Fig. 3: Comparison of experimentally measured temperatures and temperatures estimated from the theoretical model for loose (left) and compact (right) preparations of JSC-1A at a laser speed of 2.5mm/s.

Table 1: Estimated thermal diffusivity ( $k$ ), absorbed power ( $P$ ), and RMSE between model and experimental data averaged over four laser velocities.

Material	$k$ ( $m^2/s$ )	$P$ (W)	RSME
JSC-1A Loose	$2.77 \times 10^{-7}$	$5.78 \times 10^{-5}$	243
JSC-1A Compact	$6.32 \times 10^{-7}$	$9.60 \times 10^{-5}$	418
BP-1 Loose	$5.56 \times 10^{-7}$	$8.01 \times 10^{-5}$	180
BP-1 Compact	$7.83 \times 10^{-7}$	$8.40 \times 10^{-5}$	523
GRC-1 Loose	$4.49 \times 10^{-8}$	$3.70 \times 10^{-6}$	86
GRC-1 Compact	$6.91 \times 10^{-8}$	$3.90 \times 10^{-6}$	73

Four runs at different velocities were averaged together provide estimated values for  $k$  and  $P$  for loose and compact preparations of all three simulants. These values are presented in Table 1 along with the average RMSE between the model and the experimental data. A bar graph showing a comparison between estimated diffusivity values for loose and compact soil is shown in Figure 4 for each simulant. The x-offset ( $x_{off}$ ) averaged around 0.15 mm with a maximum of 0.4 mm. These low values are to be expected given that a pixel is 0.34 mm wide, and  $x_{off}$  compensates for the combination of error from pixel resolution and error caused by the theoretical maximum x value not being exactly 0.

## 5 Analysis

In all three simulants, this method produces a clear, quantifiable difference between loose and compact preparations of the same material. There are 56%, 29%, and 35% measured differences in diffusivity from the compact preparation to the loose

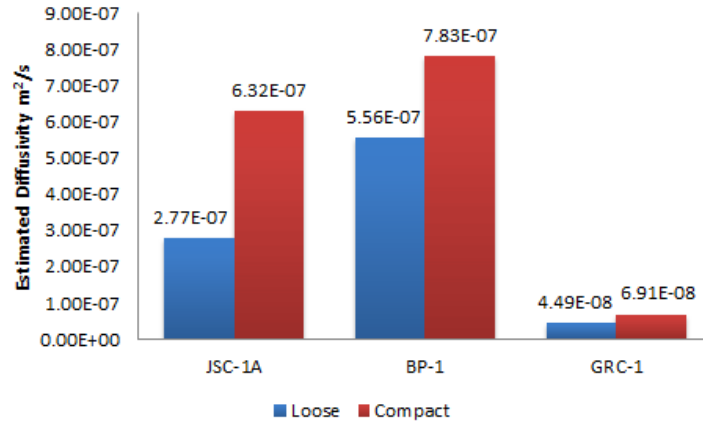


Fig. 4: Estimated thermal diffusivities ( $k$ ) of JSC-1A, BP-1, and GRC-1 averaged over four laser velocities. Demonstrates a measurable difference between compact and loose granular media.

preparation for JSC-1A, BP-1, and GRC-1, respectively. This data confirms the results expected from the theoretical model. At the speeds considered in this paper, translational velocity had no significant effect on estimated diffusivity. For example, for loose JSC-1A, (shown in Figure 5) there is only a  $9.3 \times 10^{-9}$  (2.1%) difference between the maximum and minimum estimated values. This error is within an expected range due to errors in measurement of velocity.

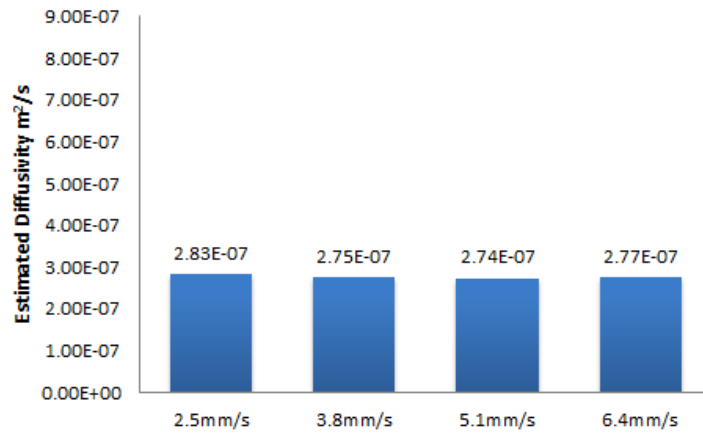


Fig. 5: Comparison of thermal diffusivity estimates for a loose preparation of JSC-1A at four different laser speeds (2.5mm/s, 3.8mm/s, 5.1mm/s, and 6.4mm/s).

As is evident in Table 1, there was some variation in  $P$  with the density of the material. This is likely due to the preparation of the soil and surface roughness, which can affect the amount of power absorbed. These results suggest that the absorbed power must be a parameter in the transient thermal model since it is dependent on properties of the material under test and difficult to predict with only a priori knowledge. The cause of this effect requires further investigation.

While the thermal diffusivity estimation method achieved similar results in each of the four trials for JSC-1A, there was slightly more variation in BP-1 and GRC-1. The variation in BP-1 was low and can be attributed to the fact that it was a non-homogeneous material with small rocks littered throughout the soil, which causes variation in its thermal properties. The variation in GRC-1 was higher. For two of the four trials, the regression algorithm found a local minimum with an incorrect value for the absorbed heat,  $P$ . When the algorithm was adjusted to limit the possible values of  $P$  for GRC-1 to a smaller interval, the method performed consistently. This error was likely caused by a lower signal to noise ratio in the signal since the temperature change in GRC-1 was significantly lower than in the other two materials. In addition, the effective spot size of the laser on GRC-1 was significantly higher than on JSC-1A and BP-1, where the spot size was close to the a priori estimated size. This is likely caused by more scattering of the light on the surface of GRC-1 than on the other two materials.

## 6 Validation with Soil Strength

Correlation between diffusivity and soil strength is validated with empirical testing using a bevameter instrument (shown in Figure 6), which emulates a mobility archetype. A bevameter performs two primary functions with high repeatability. Firstly, a sinkage test presses a flat circular plate into a soil sample while recording ground pressure exerted and linear displacement. Secondly, a shear test presses and rotates a toothed annulus while recording pressure, torque, and displacement. The intent of these functions is to mimic how a robot might sink or slip while negotiating a material [24]. As such, the end effectors are sized to reproduce the ground contact area and traction of a specific wheel (or track) design. The recording of force-displacement data produces a curve that spans robot weights and predicts sink or slip given the wheel design.

This work focused on the pressure-sinkage aspect of bevameter testing. Sinkage provides primary resistance against forward locomotion and was the primary mobility entrapment of the Spirit rover [25]. Testing here emulated the mobility system of "Red Rover" a four-wheeled, solar-powered, lunar rover prototype (shown in Figure 6). The wheels of Red Rover are sized to 300mm in diameter and are 140mm wide. Rigid aluminum construction means that the wheels do not deform to terrain under normal loads. Rule of thumb estimates for the ground contact patch on loose soil give an area of  $1832\text{mm}^2$ , which is equivalent to a 5 degree arc of the wheel. This corresponds approximately to a circular bevameter plate of 50 mm in diame-

ter. The design mass of the vehicle is 100 kg, which results in a terrestrial ground pressure of 134 kPa or a force of 245N on each wheel.



Fig. 6: A bevameter was used for measuring soil strength (right). The bevameter plate was selected to emulate Red Rover, a differential-drive lunar rover prototype (right)

Four pressure-sinkage trials were conducted on each of three test materials (BP-1, JSC-1A, GRC-1) under loose and compact preparation. In all tests, a sample approximately 18cm deep was utilized; due to edge effects, results for very high ground pressure vehicles ( $> 400\text{kPa}$ ) may be skewed for some materials. Curves for each of the parameters {soil type, compaction level} were fit from independent trials using 2nd order polynomial regression.

Experimental data shows that the estimate of thermal diffusivity is a good predictor of material resistance to rover sinkage. Figure 7 shows the pressure-sinkage curves for all materials and compaction levels tested. A lower curve indicates a stronger material and easier mobility. Results generally have high certainty for pressures under  $400\text{kPa}$ . In this range, compact BP-1 is empirically the strongest material, while both forms of GRC-1 were the weakest - resulting in greatest sinkage. The strength-order of material combinations here correspond directly to the estimated diffusivity. Results specific to the archetype rover examined in this paper are denoted with a vertical line in the graph above. It is noted that in these experiments, the sample size for materials is small and the differences in compaction level extreme. The authors do not make the leap to general applicability or existence of a linear diffusivity-strength relationship. However, these promising results warrant further investigation of the technique.

One point where bevameter data disagrees with diffusivity results is in the magnitude of phenomena resulting from compaction. It is useful to calculate the percent change in sinkage as a result of compaction, averaged over the entire range. This analysis shows that a robot would sink 235% more in loose BP-1 than in compact, 71% in JSC-1A and 26% in GRC-1. The percent changes in sinkage for JSC-1A and GRC-1 are similar to the percent changes in diffusivity. The percent change

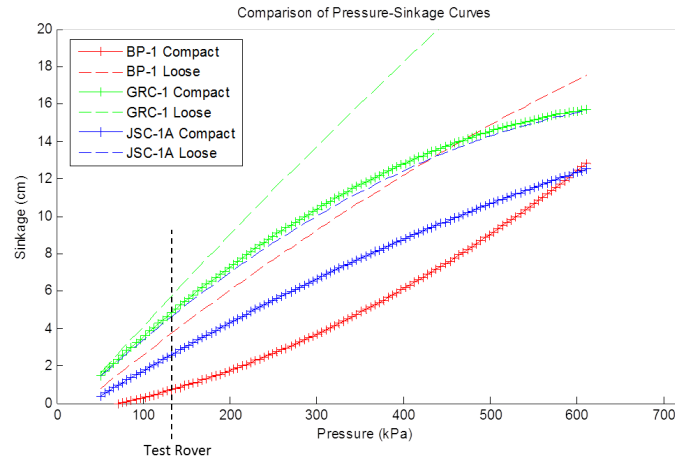


Fig. 7: Comparison of Pressure-Sinkage Curves. Curves generated for each material type and compaction level are shown. Data for the GRC-1 material is only valid for pressures under 400kPa; values beyond this are extrapolated for illustrative purposes. Performance for the rover archetype used in analysis is indicated by the vertical line at 135kPa.

in sinkage for BP-1, however, was significantly higher than the percent change in diffusivity.

For both the measurements of the pressure-sinkage relationship and the estimates of thermal diffusivity, there was significantly more variation between trials in the loose preparations than the compact preparations. This is likely in part due to the more repeatable preparation of the compact materials in comparison to the loose materials. However, it may also be because of more inherent variability in the behavior of loose granular media [26].

## 7 Conclusions and Future Work

This research developed an approach to predict the trafficability of terrain through non-contact, photothermal radiometry. The method enables differentiation between safe, compact and hazardous, loose preparations of the same soil, which vision-based methods alone cannot reliably achieve. It transmits a low-power, continuous-wave laser and thermal camera across a terrain to effect a thermal transient on terrain, measure that transient, and fit the results to an analytical model to solve for an estimate of thermal diffusivity. For each of the three simulants tested (JSC-1A, BP-1, and GRC-1), a higher measured thermal diffusivity correlated to a higher density and a stronger granular material as validated by measuring the pressure-sinkage relationship with a bevameter. Preliminary results measured a 56%, 29%, and 35% difference in diffusivity from a compact preparation to a loose preparation

for JSC-1A, BP-1, and GRC-1, respectively. These correspond to sinkage increases from compact to loose material of 71% for JSC-1A, 235% for BP-1, and 26% for GRC-1. Thus, the diffusivity estimate produced by this method is a predictor of trafficability that probes beyond the visual appearance of terrain.

Future work will analyze the efficacy of this method on mobile robots. Relative to lab instruments and conditions, robots present new challenges including the fact that the robot's velocity must be estimated in order to be able to use this method to predict trafficability. A robot's motion will also not likely be precisely linear as it was in the controlled setup used in this paper. Further work is required to adapt this technique to account for variable velocities and nonlinear trajectories. Since both the laser spot size and the temperature change induced by the laser are suspected to be influenced by terrain properties including reflectance and scattering, more research must be conducted into aiding in the estimating of those two quantities. Possibilities include using a camera to visually estimate the spot size and the magnitude of the reflected light, which is related to the amount of power absorbed by the surface. Finally, the effective depth and accuracy of this technique must be investigated in order to determine how what amount of material is actually sensed and the accuracy of the thermal diffusivity measurement.

**Acknowledgements** This work is partially supported by the NASA National Robotics Initiative program under contract NNX12AM05G. The authors would also like to thank Colin Creager and NASA Glenn Research Center for their support and for the use of the bevameter.

## References

1. K Zacny, M Bualat, P Lee, L Alvarez, T Fong, M Deans, L VanGundy, and D Lees. Using percussive, dynamic, and static soil penetrometers to assess geotechnical properties and the depth to ground ice of the mars and lunar analog terrains on the devon island, canadian arctic. In *Earth and Space 2012@ structure, and Operations in Challenging Environments*, pages 284–294. ASCE, 2012.
2. D Carrier. The four things you need to know about the geotechnical properties of lunar soil. *Lunar Geotechnical Institute*, 2005.
3. Gye-Chun Cho, Jake Dodds, and J Carlos Santamarina. Particle shape effects on packing density, stiffness, and strength: natural and crushed sands. *Journal of Geotechnical and Environmental Engineering*, 132(5):591–602, 2006.
4. Wen Li, Yong Huang, Yi Cui, Sujun Dong, and Jun Wang. Trafficability analysis of lunar mare terrain by means of the discrete element method for wheeled rover locomotion. *Journal of Terramechanics*, 47(3):161–172, 2010.
5. Nidal H Abu-Hamdeh. Thermal properties of soils as affected by density and water content. *Biosystems engineering*, 86(1):97–102, 2003.
6. Bryan R Becker, Anil Misra, and Brian A Fricke. Development of correlations for soil thermal conductivity. *International communications in heat and mass transfer*, 19(1):59–68, 1992.
7. Kathleen M Smits, Toshihiro Sakaki, Anuchit Limsuwat, and Tissa H Illangasekare. Determination of the thermal conductivity of sands under varying moisture, drainage/wetting, and porosity conditions-applications in near-surface soil moisture distribution analysis.
8. Daniel Helmick, Anelia Angelova, and Larry Matthies. Terrain adaptive navigation for planetary rovers. *Journal of Field Robotics*, 26(4):391–410, 2009.

9. WJ Parker, RJ Jenkins, CP Butler, and GL Abbott. Flash method of determining thermal diffusivity, heat capacity, and thermal conductivity. *Journal of applied physics*, 32(9):1679–1684, 1961.
10. WP Leung and AC Tam. Techniques of flash radiometry. *Journal of applied physics*, 56(1):153–161, 1984.
11. AC Tam and B Sullivan. Remote sensing applications of pulsed photothermal radiometry. *Applied Physics Letters*, 43(4):333–335, 1983.
12. Alonzo Kelly, Anthony Stentz, Omead Amidi, Mike Bode, David Bradley, Antonio Diaz-Calderon, Mike Happold, Herman Herman, Robert Mandelbaum, Tom Pilarski, et al. Toward reliable off road autonomous vehicles operating in challenging environments. *The International Journal of Robotics Research*, 25(5-6):449–483, 2006.
13. S. Chhaniyara, C. Brunskill, B. Yeomans, M.C. Matthews, C. Saaj, S. Ransom, and L. Richter. Terrain trafficability analysis and soil mechanical property identification for planetary rovers: A survey. *Journal of Terramechanics*, 49(2):115 – 128, 2012.
14. H. E. Cline and T. R. Anthony. Heat treating and melting material with a scanning laser or electron beam. *Journal of Applied Physics*, 48(9):3895–3900, 1977.
15. Inan Chen and Sanboh Lee. Transient temperature profiles in solids heated with scanning laser. *Journal of Applied Physics*, 54(2):1062–1066, 1983.
16. H.S. Carslaw and J. C. Jaeger. *Conduction of heat in solids*. Oxford University Press, Oxford, 1959.
17. Richard Haberman. *Elementary applied partial differential equations: with Fourier series and boundary value problems*. Prentice-Hall Englewood Cliffs, NJ, 1987.
18. D. J. Sanders. Temperature distributions produced by scanning gaussian laser beams. *Appl. Opt.*, 23(1):30–35, Jan 1984.
19. J. E. Moody and R. H. Hendel. Temperature profiles induced by a scanning cw laser beam. *Journal of Applied Physics*, 53(6):4364–4371, 1982.
20. J. M. Liu. Simple technique for measurements of pulsed gaussian-beam spot sizes. *Opt. Lett.*, 7(5):196–198, May 1982.
21. Xiangwu Zeng, Chunmei He, Heather Oravec, Allen Wilkinson, Juan Agui, and Vivake Asnani. Geotechnical properties of jsc-1a lunar soil simulant. *Journal of Aerospace Engineering*, 23(2):111–116, 2009.
22. DB Stoesser, DL Rickman, and S Wilson. Preliminary geological findings on the bp-1 simulant. 2010.
23. HA Oravec, X Zeng, and VM Asnani. Design and characterization of grc-1: A soil for lunar terramechanics testing in earth-ambient conditions. *Journal of Terramechanics*, 47(6):361–377, 2010.
24. JY Wong. Theory of ground vehicles, 2001. *John Wiley&Sons*.
25. Jo Yung Wong. *Terramechanics and off-road vehicle engineering: terrain behaviour, off-road vehicle performance and design*. Butterworth-Heinemann, 2009.
26. Krzysztof Skonieczny. *Lightweight Robotic Excavation*. PhD thesis, Carnegie Mellon University, 2013.